

# SCIENTIFIC REPORTS

OPEN

## Materials analysis and focused ion beam nanofabrication of topological insulator $\text{Bi}_2\text{Se}_3$

Sarah Friedensen , Jerome T. Mlack & Marija Drndić

Focused ion beam milling allows manipulation of the shape and size of nanostructures to create geometries potentially useful for opto-electronics, thermoelectrics, and quantum computing. We focus on using the ion beam to control the thickness of  $\text{Bi}_2\text{Se}_3$  and to create nanowires from larger structures. Changes in the material structure of  $\text{Bi}_2\text{Se}_3$  nanomaterials that have been milled using a focused ion beam are presented. In order to characterize the effects of ion beam processing on the samples, we use a variety of techniques including analytical transmission electron microscopy and atomic force microscopy. The results show that while part of the material remains intact after shaping, amorphous regions form where the beam has been used to thin the sample. For wires created by thinning the material down to the substrate, the sidewalls of the wires appear intact based on diffraction images from samples cut at an angle, but thin crystalline regions remain at the wire edges. Even with the resulting defects and limitations when thinning, focused ion beam milling can be used to fabricate custom geometries of  $\text{Bi}_2\text{Se}_3$  nanostructures.

In the field of nanoelectronics some of the most interesting device proposals require the control of nanostructure properties, especially the shape and size. In the case of nanodevices made from topological insulators, such as bismuth selenide ( $\text{Bi}_2\text{Se}_3$ ), proposals exist for observing exotic phenomena that could have far-reaching applications, including fault-tolerant quantum computing using Majorana fermions<sup>1–7</sup> and dramatic increases in thermoelectric efficiency<sup>8–13</sup>. These proposals require the ability to fabricate structures such as wires with well-controlled dimensions<sup>1,12</sup>, antidot lattices with specific spacings<sup>9,10</sup>, and carefully patterned defects<sup>11,14,15</sup>. Directly growing nanostructures bottom-up into the necessary geometries and defect densities would be ideal, but controlled growth and scaling of such devices is complicated. An alternative is to use top-down methods, such as ion milling, to modify the  $\text{Bi}_2\text{Se}_3$ <sup>16–25</sup>.

In this article, we focus on the use of gallium-based focused ion beam (FIB) milling, diagramed in Fig. 1. FIB milling utilizes  $\text{Ga}^+$  ions to sputter away a target material and can be used to both sculpt the material<sup>16,17,21,22</sup> and introduce defects<sup>18,21</sup>. Recent transport studies have shown that FIB-created nanowires of  $\text{Bi}_2\text{Se}_3$  exhibit increased photoconductivity at room temperature<sup>22</sup> and retain signatures of their topological surface states at low temperature<sup>16,17</sup>. The low-temperature transport results indicate, however, that the nanowires are not entirely  $\text{Bi}_2\text{Se}_3$  and that the crystal structure has been partially altered by the FIB<sup>16</sup>. While these results are encouraging for FIB milling as a method of top-down fabrication of  $\text{Bi}_2\text{Se}_3$ , they do not fully address the materials analysis and changes in the material structure. Therefore, in order to better understand the effects of FIB imaging and modification on  $\text{Bi}_2\text{Se}_3$ , we have fabricated nanostructures via thinning and cutting with the ion beam and analyzed the material changes. In our study, we combine transmission electron microscopy (TEM) methods—such as energy dispersive x-ray spectroscopy (EDS) and selected area diffraction (SAED)—with atomic force microscopy (AFM).

### Results

An AFM map of a FIB-milled  $\text{Bi}_2\text{Se}_3$  flake on a  $\text{SiO}_2$  substrate is shown in Fig. 2(a). Multiple  $4 \mu\text{m}^2$  regions of the flake were exposed to the ion beam, each for a different length of time. The shortest mill time was 4 seconds, and the longest was 28 seconds. All milled regions have a roughness of less than 1 nm, which indicates uniform milling across each area. In comparison, Argon plasma etching<sup>23</sup> creates surfaces with roughness greater than 2 nm for any etch time over a few seconds. Figure 2(b), which shows the dose in units of seconds per unit area versus etch

Department of Physics and Astronomy, University of Pennsylvania, Philadelphia, Pennsylvania 19104, USA. Sarah Friedensen and Jerome T. Mlack contributed equally to this work. Correspondence and requests for materials should be addressed to M.D. (email: [drndic@physics.upenn.edu](mailto:drndic@physics.upenn.edu))

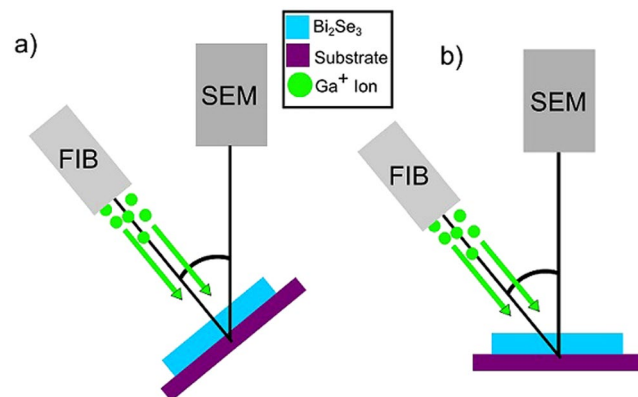


**Figure 1.** Diagram of FIB milling setup. (a) With  $\text{Bi}_2\text{Se}_3$  flake aimed toward FIB beam for straight-on milling. (b) With  $\text{Bi}_2\text{Se}_3$  flake angled away from FIB beam for angled milling.

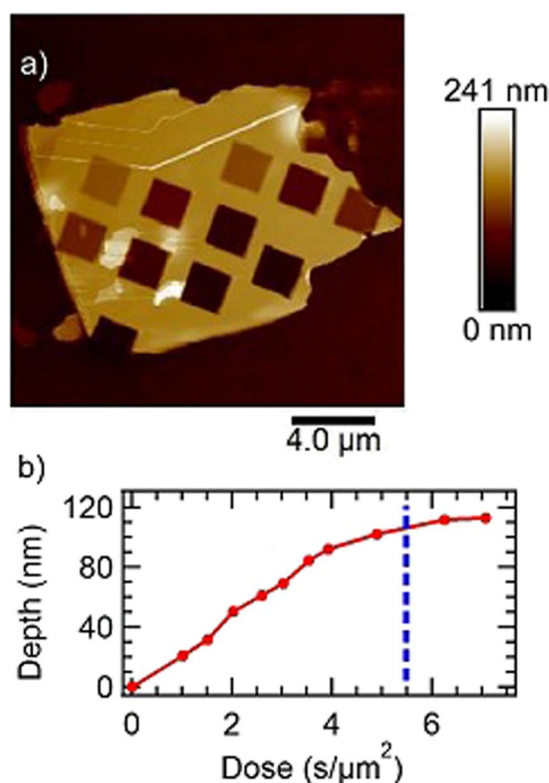


**Figure 2.**  $\text{Bi}_2\text{Se}_3$  flake thinned using focused ion beam at 10 pA setting. (a) AFM image of FIB thinned  $\text{Bi}_2\text{Se}_3$  on silicon oxide substrate. Each square is approximately  $4 \mu\text{m}^2$  in area. (b) Plot of depth as a function of FIB beam dose. Dashed blue line represents the approximate dose at which the beam has milled through the  $\text{Bi}_2\text{Se}_3$  and begun milling the silicon oxide.

depth, was calculated from the map in Fig. 2(a). The mill-rate appears constant until a depth of 110 nm, which is indicated by a vertical blue dashed line. Below this depth, the FIB had milled beyond the  $\text{Bi}_2\text{Se}_3$  and was milling the underlying substrate. The linearity of the mill depth vs. dose before this point suggests that there was minimal sample heating during the exposure times used.

Figure 3 presents EDS and SAED analysis of a FIB-thinned sample on a silicon nitride TEM window. The silicon nitride windows are advantageous because they have a featureless SAED pattern and only contribute Si and N signals to the EDS measurement. A sample SAED pattern for a silicon nitride window is shown in Supplement Fig. S5.1. Figure 3(a) shows a counts per second image of an exfoliated and milled  $\text{Bi}_2\text{Se}_3$  flake. Regions of the flake that were not milled are highlighted in green. The total ion doses used for each region are noted in Supplement Fig. S2.1 and range from  $10^{15} \text{ cm}^{-2}$  to  $2 \times 10^{16} \text{ cm}^{-2}$ . The effect of ion milling on the flake is evident in both the brightness of the stripes in the image and in the x-ray counts in the EDS line scan (path

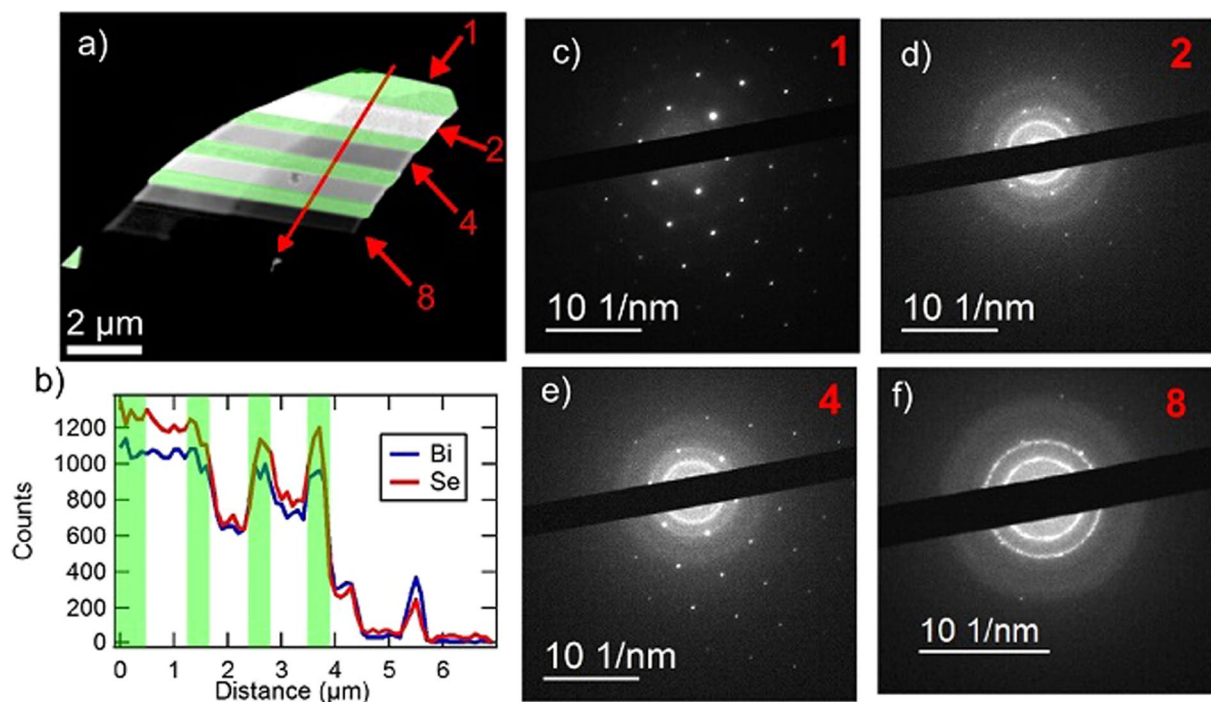


**Figure 3.** TEM image, EDS trace, and selected area diffraction spots from selected regions on a  $\text{Bi}_2\text{Se}_3$  flake thinned using the focused ion beam at the 10 pA setting. SAED patterns from all regions are shown in Supplement Fig. S2.2. (a) Counts per second image of thinned  $\text{Bi}_2\text{Se}_3$  flake. (b) Trace of EDS intensities of Bi (blue) and Se (red) across the sample as represented with a red arrow crossing the sample in (a). (c) Diffraction from bulk region, region 1 in (a). (d) Diffraction from region thinned for 1 second, region 2 in (a). (e) Diffraction from region thinned for 5 seconds, region 4 in (a). (f) Diffraction from region thinned for 10 seconds, region 8 in (a).

indicated by a red line across the sample in Fig. 3(a), as shown in Fig. 3(b). The green regions in Fig. 3(b) again denote the unmilled regions. The first milled region, which received an ion dose of  $10^{15} \text{ cm}^{-2}$ , shows minimal change in Se:Bi count ratio. Regions subjected to higher doses show a decrease in the Se:Bi ratio, which indicates preferential removal of Se. This is expected due to Se's lower mass. The decrease in the ratio is most extreme in the small amount of leftover material at a horizontal distance  $5.5 \mu\text{m}$  from the start of the line scan. At this position, the Bi signal dominates. EDS signatures from Ga were observed only in the areas below region 8, which has been milled down below a thickness of 10 nm. This suggests that the Ga ions largely pass through the  $\text{Bi}_2\text{Se}_3$  and become embedded in the silicon nitride. SAED images from several bands across the flake are shown in Fig. 3(c–f). Figure 3(c) is from the top un-etched region, labeled 1 in Fig. 3(a), and shows a hexagonal diffraction pattern consistent with bulk  $\text{Bi}_2\text{Se}_3$ . The SAED images from regions 2 and 4, Fig. 3(d) and (e) respectively, show both the hexagonal pattern and a distinct ring with a diameter of  $6.3 \text{ nm}^{-1}$ . The diffraction pattern from region 8 shows both the  $6.3 \text{ nm}^{-1}$  ring and some evidence of polycrystalline  $\text{Bi}_2\text{Se}_3$ . The polycrystalline structure is indicated by a ring of spots with a diameter of  $9.1 \text{ nm}^{-1}$ , which corresponds to a lattice spacing of 0.22 nm. The  $6.3 \text{ nm}^{-1}$  diameter ring in the milled regions suggests that milling creates an amorphous surface. Given the decrease in the Se:Bi ratio, the surface is likely primarily Bi. The ring diameter equates to a lattice spacing of 0.32 nm, which means the surface could correspond to a bismuth oxide layer formed from air exposure after FIB milling<sup>26,27</sup> or recrystallized bismuth<sup>28,29</sup>.

Results from sculpting and milling wires from a flake are presented in Fig. 4. Figure 4(a) shows a counts per second EDS image of a sample milled to make eight wires of varying widths, from 260 nm to 26 nm. Areas in which the beam etched entirely through the  $\text{Bi}_2\text{Se}_3$  and into the silicon nitride appear as lighter gray regions in between the wires. The lighter color is indicative of Ga embedded in the substrate. Elemental maps of the Ga, Se, and Bi in the sample are presented in Supplement Fig. S3.1. Numbered 1–4 in the image are wires selected for further analysis. Figure 4(b) shows the diffraction pattern from the bulk  $\text{Bi}_2\text{Se}_3$  region of the flake with the selected area inset. SAED from wires 1–4 are shown in Fig. 4(c–f) respectively, with the selected areas inset. As the wires decrease in width, the  $\text{Bi}_2\text{Se}_3$  diffraction spots disappear. For wire 3 (width 120 nm) only one pair of blurred  $\text{Bi}_2\text{Se}_3$  diffraction spots is visible, and for wire 4 (width 26 nm) none are visible. The disappearance of these diffraction spots combined with the emergence of spots with a spacing similar to the thinned regions from Fig. 2, suggests that as the wire width decreases, defected or recrystallized material makes up a larger proportion of the wire. The edge regions could be the result of recrystallization of incompletely sputtered materials or the formation of an oxide, diagrammed in Supplement Figure S1.1.

The destruction of the  $\text{Bi}_2\text{Se}_3$  as a function of wire width is further evidenced by the EDS elemental mapping shown in Fig. 4(g). In the map, blue areas represent regions containing Bi/Se/Si, and the red areas represent Si

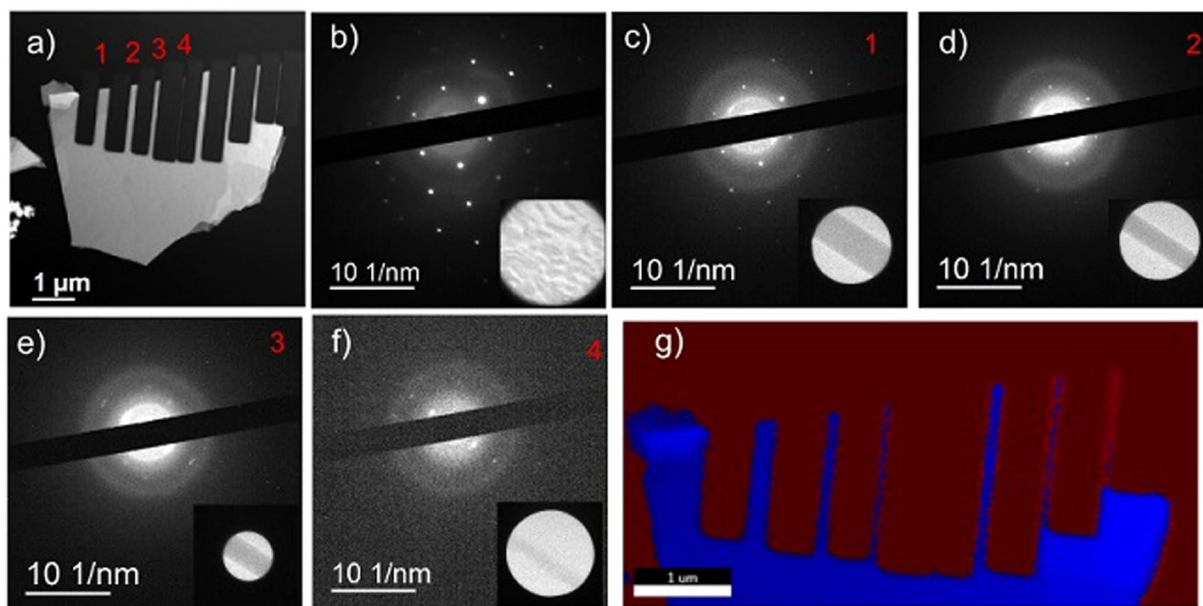


**Figure 4.**  $\text{Bi}_2\text{Se}_3$  sample cut into wires with diffraction and EDS imaging. (a) Counts per second image of  $\text{Bi}_2\text{Se}_3$  wire sample. (b) SAED pattern, and inset image, of unaltered  $\text{Bi}_2\text{Se}_3$  region. (c) SAED of wire 1, width of 260 nm, with inset of selected region. (d) SAED of wire 2, width of 160 nm, with inset of selected region. (e) SAED of wire 3, width of 120 nm, with inset of selected region. (f) SAED of wire 4, width of 26 nm, with inset of selected region. (g) EDS map of wire sample, blue represents regions containing Bi and Se and red represents their absence.

only. The Ga signal, while observable in an elemental map, is low enough that the EDS software does not distinguish it in the phase maps. As can be seen in the map, wire 4 is not distinguishable from the substrate. This indicates that although some material remains, as shown in the counts per second image, the wire may no longer be  $\text{Bi}_2\text{Se}_3$ . This supports what was observed in the diffraction pattern in Fig. 4(f), which shows no evidence of a  $\text{Bi}_2\text{Se}_3$  crystal structure. These results are comparable to the transport results in Bhattacharyya *et al.*<sup>16</sup>. In that article, the authors observe Ahnranov-Bohm oscillations in FIB-cut nanowires that show a period associated with wire cross-sections smaller than their physical cross-sections, indicating damage to the wires from the FIB milling. The authors suggested this was due to deformations/cracking or  $\text{Ga}^+$  ion implantation; our results suggest that the dominant factor is defect creation, which is supported by the minimal Ga signal in the EDS of the thinned sample and by the disappearance of the  $\text{Bi}_2\text{Se}_3$  diffraction spots as a function of width in the wires. It should also be noted that we observe no evidence of large scale cracking from the ion milling, which would appear as splitting in the SAED pattern and as visible cracks in the TEM images of the wires.

In order to look more carefully at the material along the wire edges and the structure of wire 4, we collected high resolution TEM (HRTEM) images. These images and their fast Fourier transforms (FFT) are shown in Fig. 5. The HRTEM image of the edge of wire 2 is shown in Fig. 5(a) and its FFT is shown inset. We define the wire “edge” as the approximately 20 nm-wide region in from the physical edge of the wire (denoted in Fig. 5(a) with dashed lines). The difference between the edge region and bulk is represented in Fig. 5(b) and (c), which show FFTs from the interior (red) and edge region (blue) respectively. The FFT in Fig. 5(b) shows a hexagonal pattern with lattice spacing similar to bulk. The edge region, Fig. 5(c), shows a single pair of lattice spots with a lattice spacing of 0.3 nm. This indicates a different crystal structure than  $110 \text{ Bi}_2\text{Se}_3$ . A similar treatment of wire 4, whose width is on the order of the edge region observed in larger wires, is shown in Fig. 5(d) and (e), an HRTEM image and its FFT respectively. While a pair of  $\text{Bi}_2\text{Se}_3$  diffraction spots is observed, they are not the dominant signal. Inspection of the HRTEM images reveals islands of bismuth selenide lattice in wire 4, but they are isolated from each other and make up only a small fraction of the material in the wire. Instead, lattice planes similar to those observed at the edges of other wires and milled regions dominate.

This further supports the results from Fig. 4(f) and (g). The FFT and HRTEM images of the wire edges indicate that while some crystal order exists, the edges are largely not  $\text{Bi}_2\text{Se}_3$ . This material could be a bismuth oxide<sup>26,27</sup> or crystalline bismuth<sup>28,29</sup>, similar to that suggested by the thinning results. However, the material by the edge may not directly reflect the edge itself.

To study the effect of the ion beam on the edges it creates during milling, without the interference of excess material, a sample was milled at an angle. The angle cutting will sputter material away from the sample leaving a surface which has been minimally affected by the beam, as illustrated in the Supplement S1.1. The TEM and AFM results from this sample are shown in Fig. 6. The red circle on the TEM image in Fig. 6(a) highlights the primary analyzed region, though the sample was milled in multiple locations. In this region the beam was incident from right of the sample at an angle of  $52^\circ$  from the substrate normal. Figure 6(b) shows the diffraction from this region, with the selected area shown in the inset. The diffraction pattern from this area is hexagonal and has a



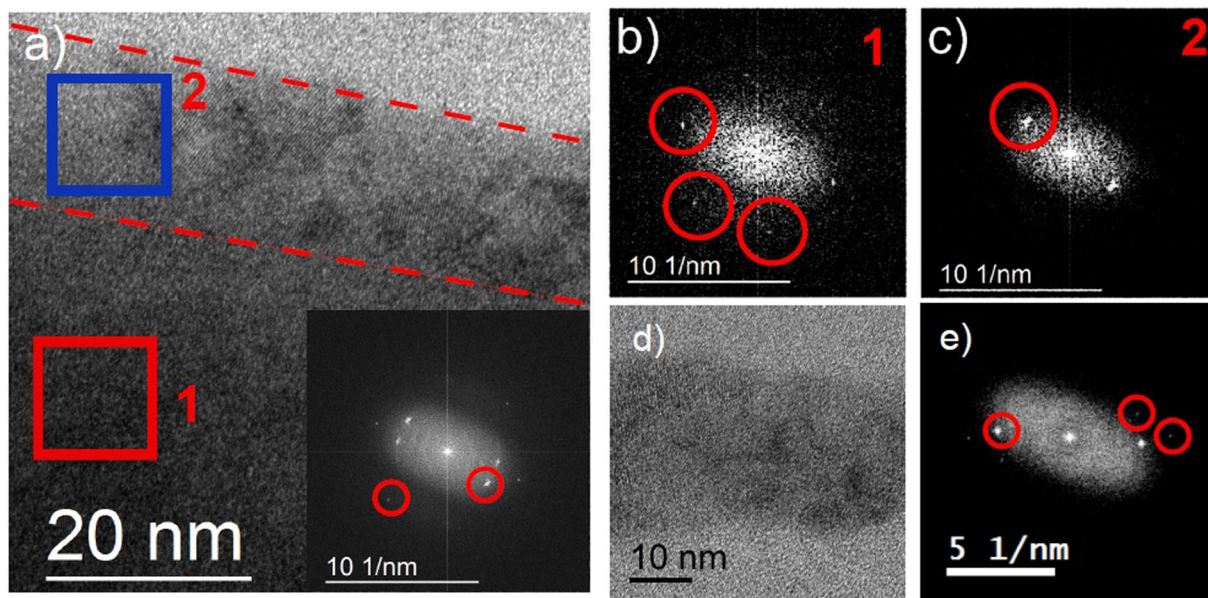


**Figure 5.** High resolution TEM and FFT images of wires. (a) HRTEM image of wire 2 from Fig. 4(a), edge of the wire is denoted between dashed red lines. Inset is FFT of entire image. (b) FFT of region 1 (red box) from (a). (c) FFT of region 2 (blue box) from (a). (d) HRTEM image of edge of wire 4 from Fig. 4(a). (e) FFT of (d).

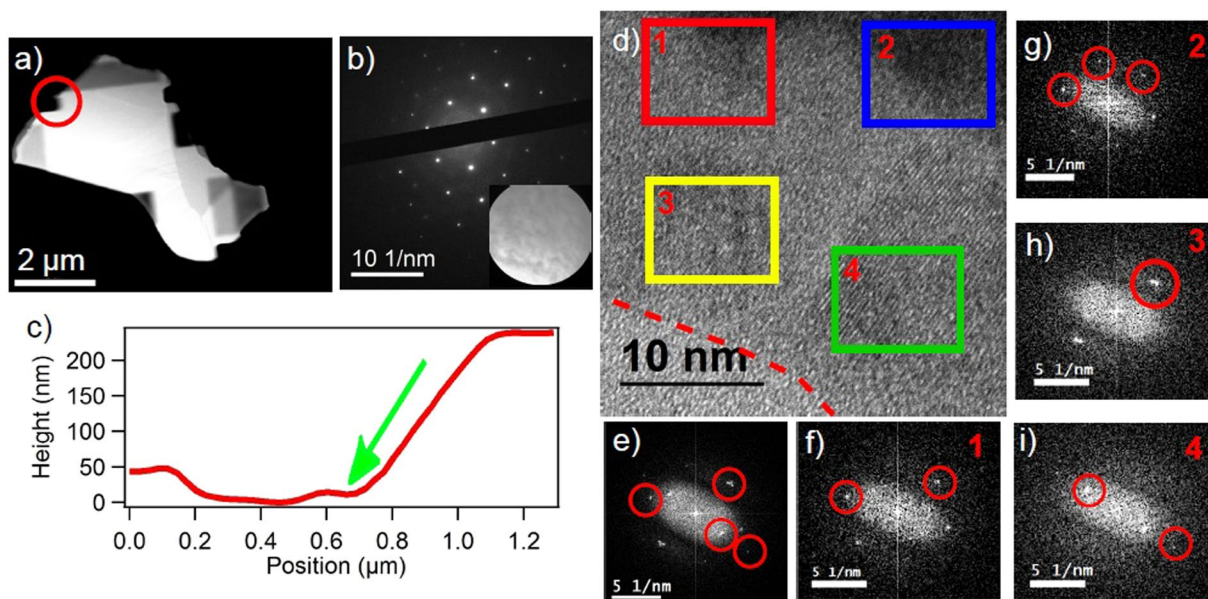


**Figure 6.** TEM and FFT images and analysis of  $\text{Bi}_2\text{Se}_3$  flake cut at a  $52^\circ$  angle from the substrate normal. (a) TEM image of angle-cut flake. (b) SAED image of region circled in red in (a). Inset is the image of the actual area selected for taking diffraction. (c) Height versus position slice from FIB cut region circled in red in (a). Green arrow indicates the approximate direction of the beam relative to the sample. (d) HRTEM image from a region in the circled region in (a) at end of milled region, red-dashed line indicates where image and FFT no longer show any evidence of crystalline structure. (e) FFT of entire image in (d). (f) FFT of region 1 (red box) in (d). (g) FFT of region 2 (blue box) in (d). (h) FFT of region 3 (yellow box) in (d). (i) FFT of region 4 (green box) in (d).

lattice parameter of 0.21 nm. Unlike the thinned regions presented in Fig. 3, no amorphous rings appear, which indicates the angle-cut surface is minimally damaged and nominally indistinguishable from un-milled  $\text{Bi}_2\text{Se}_3$ . In an AFM slice of this region (Fig. 6(c)), we find that the dose from the beam (direction shown by the green arrow), was also able to mill into the silicon nitride window. The surface of the cut is smooth, and the angle of the cut relative to the substrate normal is  $58^\circ$ . The higher angle of the cut indicates that some material was removed in excess.

To better investigate the thinnest regions of the cut where the highest proportion of defected material to  $\text{Bi}_2\text{Se}_3$  is located we analyze the HRTEM of thinned region, shown in Fig. 6(d). The FFT of this entire region, Fig. 6(e), shows multiple lattice spots corresponding to multiple crystal phases, including  $\text{Bi}_2\text{Se}_3$ , unlike the diffraction, which shows only  $\text{Bi}_2\text{Se}_3$  spots. The FFTs from specific regions in this sample, shown as boxes in Fig. 6(d), illustrate the transition from regions where the  $\text{Bi}_2\text{Se}_3$  structure is dominant (thicker regions) to the end of the cut where the structure varies (at approximately the 800 nm position in Fig. 6(c)). The end of the cut is denoted by the red dashed line in Fig. 6(d) and is the point after which no spots or order is observed in the image or FFT. The top two thicker regions, Fig. 6(f) and (g), clearly show the  $\text{Bi}_2\text{Se}_3$  lattice spots in the FFT with a spacing close to the bulk value and show the hexagonal pattern. The regions close to the end show very different patterns. Specifically, Fig. 6(h) shows two pair of nearly superimposed lattice spots with a lattice spacing similar to  $\text{Bi}_2\text{Se}_3$ , while Fig. 6(i) shows the previously observed lattice spacing of 0.3 nm. This shows that in the thinner regions near the physical edge, crystalline  $\text{Bi}_2\text{Se}_3$  coexists with another crystalline phase or phases that are not observed in thicker regions. The results from all four regions show that even though the flake has been cut by the FIB beam, the face of the cut has not been greatly affected. Thus, the “edge” regions from the wires were most likely leftover material from the top down milling, and the sidewalls were not affected in an observable way using our methods.

## Discussion

In conclusion, FIB milling of  $\text{Bi}_2\text{Se}_3$  shows promise as method for sculpting this topological insulator to create application-specific geometries. While FIB-thinning the sample creates a uniform and smooth surface, it also damages the material and creates regions that are Se-deficient and partially amorphous. The edges created when cutting wires in the  $\text{Bi}_2\text{Se}_3$  are smooth, and their diffraction patterns are indistinguishable from bulk regions as shown via HRTEM and cutting samples at an angle. The excess edge material from direct exposure is shown to be crystalline, but the exact nature of this material was not determinable in this study. The quality of the wires decreased below a width of approximately 150 nm. Smaller wires that maintain the  $\text{Bi}_2\text{Se}_3$  crystal may be achievable, however, depending on the characteristics of the FIB tool. Overall, FIB milling of  $\text{Bi}_2\text{Se}_3$  nanostructures has some limitations highlighted here, but is an overall promising and easy method for manufacturing nanostructures.

## Methods

**Nanostructure Transfer.** Nanostructures were mechanically exfoliated from bulk  $\text{Bi}_2\text{Se}_3$  obtained from Alfa Aesar (99.999% purity). For  $\text{Bi}_2\text{Se}_3$  samples on  $\text{SiO}_2$ , they were directly exfoliated onto the substrate. For samples on silicon nitride membranes, the  $\text{Bi}_2\text{Se}_3$  was exfoliated onto PMMA, then positioned and transferred onto a 100 nm thick membrane substrate using a micromanipulator and microscope method outlined in Mlack *et al.*<sup>30</sup>. After positioning, acetone was used to remove the PMMA and complete the transfer of the  $\text{Bi}_2\text{Se}_3$  to the membrane. In between all measurements, samples were stored in a vacuum desiccator to reduce the effects of oxidation.

**FIB Milling.** The samples were milled using a FEI Strata DB235 focused ion beam at 30 kV and 10 pA beam current setting.

**TEM Measurement.** The samples were analyzed using a JEOL 2010F TEM operating at 200 kV. Samples were measured in both cases where the chip is face up (sample hit by beam first) and face down (sample hit by beam through nitride window), as depicted in the Supplement S4.1. This is primarily important for obtaining HRTEM images (best face down) and EDS (best face up to maximize signal to detector). For SAED images, the nitride window has a minimal effect as it merely adds an amorphous background. SAED of nitride is shown in Supplement S5.1. The images, EDS, and diffraction in Figs. 2, 3, S2.2, S3.1, and S3.2 were taken in the face-up position and all others in the face-down position. The FFTs from the HRTEM images were processed using Gatan Digital Micrograph.

**AFM Measurement.** The AFM was a Bruker Icon atomic force microscope operated in tapping mode.

## References

- Ilan, R., Bardarson, J. H., Sim, H.-S. & Moore, J. E. Detecting perfect transmission in Josephson junctions on the surface of three dimensional topological insulators. *New Journal of Physics* **16**, 053007, <https://doi.org/10.1088/1367-2630/16/5/053007> (2014).
- Fu, L. & Kane, C. L. Superconducting proximity effect and Majorana fermions at the surface of a topological insulator. *Phys. Rev. Lett.* **100**, 096407–096411, <https://doi.org/10.1103/PhysRevLett.100.096407> (2008).
- Akhmerov, A. R., Nilsson, J. & Beenakker, C. W. J. Electrically detected interferometry of Majorana fermions in a topological insulator. *Phys. Rev. Lett.* **102**, 216404, <https://doi.org/10.1103/PhysRevLett.102.216404> (2009).
- Hsieh, T. H. & Fu, L. Majorana fermions and exotic surface Andreev bound states in topological superconductors: Application to  $\text{Cu}_x\text{Bi}_2\text{Se}_3$ . *Phys. Rev. Lett.* **108**, 107005, <https://doi.org/10.1103/PhysRevLett.108.107005> (2012).
- Beenakker, C. W. J. Search for Majorana fermions in superconductors. In Langer, J. (ed.) *Annual Review of Condensed Matter Physics*, vol. 4, 113–136 (Annual Reviews, 2013).
- Kitaev, A. Fault-tolerant quantum computation by anyons. *Annals of Physics* **303**, 2–30, [https://doi.org/10.1016/S0003-4916\(02\)00018-0](https://doi.org/10.1016/S0003-4916(02)00018-0) (2003).
- Nayak, C., Simon, S. H., Stern, A., Freedman, M. & Das Sarma, S. Non-abelian anyons and topological quantum computation. *Rev. Mod. Phys.* **80**, 1083–1159, <https://doi.org/10.1103/RevModPhys.80.1083> (2008).
- Sun, G. L. *et al.* Enhanced thermoelectric performance of nanostructured topological insulator  $\text{Bi}_2\text{Se}_3$ . *Applied Physics Letters* **106**, <https://doi.org/10.1063/1.4907252> (2015).
- Tretiakov, O. A., Abanov, A. & Sinova, J. Thermoelectric efficiency of topological insulators in a magnetic field. *Journal of Applied Physics* **111**, <https://doi.org/10.1063/1.3672847> (2012).
- Tretiakov, O. A., Abanov, A. & Sinova, J. Holey topological thermoelectrics. *Applied Physics Letters* **99**, <https://doi.org/10.1063/1.3637055> (2011).

11. Shi, H., Parker, D., Du, M.-H. & Singh, D. J. Connecting thermoelectric performance and topological-insulator behavior:  $\text{Bi}_2\text{Te}_3$  and  $\text{Bi}_2\text{Se}_3$  from first principles. *Phys. Rev. Applied* **3**, 014004, <https://doi.org/10.1103/PhysRevApplied.3.014004> (2015).
12. Shin, H. S. *et al.* The surface-to-volume ratio: a key parameter in the thermoelectric transport of topological insulator  $\text{Bi}_2\text{Se}_3$  nanowires. *Nanoscale* **8**, 13552–13557, <https://doi.org/10.1039/C6NR01716A> (2016).
13. Wu, K., Ramachandran, B., Kuo, Y., Sankar, R. & Chou, F. Influence of induced defects on transport properties of the bridgman-grown  $\text{Bi}_2\text{Se}_3$ -based single crystals. *Journal of Alloys and Compounds* **682**, 225–231, <https://doi.org/10.1016/j.jallcom.2016.04.306> (2016).
14. Sacksteder, V., Ohtsuki, T. & Kobayashi, K. Modification and control of topological insulator surface states using surface disorder. *Phys. Rev. Applied* **3**, 064006, <https://doi.org/10.1103/PhysRevApplied.3.064006> (2015).
15. Philip, T. M., Hirsbrunner, M. R., Park, M. J. & Gilbert, M. J. Performance of topological insulator interconnects. *IEEE Electron Device Letters* **38**, 138–141, <https://doi.org/10.1109/LED.2016.2629760> (2017).
16. Bhattacharyya, B. *et al.* Observation of quantum oscillations in fib fabricated nanowires of topological insulator ( $\text{Bi}_2\text{Se}_3$ ). *Journal of Physics Condensed Matter* **29**, <https://doi.org/10.1088/1361-648X/aa5536> (2017).
17. Bhattacharyya, B., Sharma, A., Awana, V., Senguttuvan, T. & Husale, S. Fib synthesis of  $\text{Bi}_2\text{Se}_3$  1d nanowires demonstrating the co-existence of shubnikov-de haas oscillations and linear magnetoresistance. *Journal of Physics Condensed Matter* **29**, <https://doi.org/10.1088/1361-648X/29/7/07LT01> (2017).
18. Sharma, P. A. *et al.* Ion beam modification of topological insulator bismuth selenide. *Applied Physics Letters* **105**, <https://doi.org/10.1063/1.4904936> (2014).
19. Zhou, W., Zhu, H., Valles, C. M. & Yarmoff, J. A. Preparation of clean surfaces and Se vacancy formation in  $\text{Bi}_2\text{Se}_3$  by ion bombardment and annealing. *Surface Science* **662**, 67–73, <https://doi.org/10.1016/j.susc.2017.04.004> (2017).
20. Tan, Y. *et al.* Tailoring nonlinear optical properties of  $\text{Bi}_2\text{Se}_3$  through ion irradiation. *Scientific Reports* **6**, <https://doi.org/10.1038/srep21799> (2016).
21. Fukui, N. *et al.* *in situ* microfabrication and measurements of  $\text{Bi}_2\text{Se}_3$  ultrathin films in a multichamber system with a focused ion beam, molecular beam epitaxy, and four-tip scanning tunneling microscope. *e-Journal of Surface Science and Nanotechnology* **12**, 423–430, <https://doi.org/10.1380/ejssnt.2014.423> (2014).
22. Sharma, A., Bhattacharyya, B., Shrivastava, A. K., Senguttuvan, T. D. & Husale, S. High performance broadband photodetector using fabricated nanowires of bismuth selenide. *Scientific Reports* **6**, <https://doi.org/10.1038/srep19138> (2016).
23. Childres, I., Tian, J., Miotkowski, I. & Chen, Y. Afm and raman studies of topological insulator materials subject to argon plasma etching. *Philosophical Magazine* **93**, 681–689, <https://doi.org/10.1080/14786435.2012.728009> (2013).
24. Saji, A., Ampili, S., Yang, S.-H., Ku, K. J. & Elizabeth, M. Effects of doping, electron irradiation,  $\text{h}^+$  and  $\text{he}^+$  implantation on the thermoelectric properties of  $\text{Bi}_2\text{Se}_3$  single crystals. *Journal of Physics: Condensed Matter* **17**, 2873, <https://doi.org/10.1088/0953-8984/17/19/005> (2005).
25. Jia, G., Wu, Z., Wang, P., Yao, J. & Chang, K. Morphological evolution of self-deposition  $\text{Bi}_2\text{Se}_3$  nanosheets by oxygen plasma treatment. *Scientific Reports* **6**, <https://doi.org/10.1038/srep22191> (2016).
26. Wang, Y., Jiang, L., Tang, D., Liu, F. & Lai, Y. Characterization of porous bismuth oxide ( $\text{Bi}_2\text{O}_3$ ) nanoplates prepared by chemical bath deposition and post annealing. *RSC Adv.* **5**, 65591–65594, <https://doi.org/10.1039/C5RA09949H> (2015).
27. In, J. *et al.* Polymorph-tuned synthesis of  $\alpha$  and  $\beta$   $\text{Bi}_2\text{O}_3$  nanowires and determination of their growth direction from polarized raman single nanowire microscopy. *Chemistry - A European Journal* **17**, 1304–1309, <https://doi.org/10.1002/chem.201001684> (2011).
28. Chen, J., Wu, L.-M. & Chen, L. Syntheses and characterizations of bismuth nanofilms and nanorhombuses by the structure-controlling solventless method. *Inorganic Chemistry* **46**, 586–591, <https://doi.org/10.1021/ic0615067> (2007).
29. Chang, X. *et al.* Insights into the growth of bismuth nanoparticles on 2d structured biocl photocatalysts: an *in situ* tem investigation. *Dalton Trans.* **44**, 15888–15896, <https://doi.org/10.1039/C5DT02217G> (2015).
30. Mlack, J. T. *et al.* Transfer of monolayer  $\text{WSe}_2$  and raman study of substrate effects. *Scientific Reports* **7**, <https://doi.org/10.1038/srep43037> (2017).

## Acknowledgements

This work was supported under by the National Science Foundation through the grant EFRI 2-DARE 1542707. Use of University of Pennsylvania Nano/Bio Interface Center instrumentation is acknowledged.

## Author Contributions

J.T.M., S.F., and M.D. devised experiments. J.T.M. and S.F. prepared samples. J.T.M. performed FIB milling. S.F. performed AFM and TEM measurement. J.T.M. analyzed AFM and TEM data and prepared all figures and results discussion. All authors contributed to the manuscript preparation.

## Additional Information

**Supplementary information** accompanies this paper at <https://doi.org/10.1038/s41598-017-13863-6>.

**Competing Interests:** The authors declare that they have no competing interests.

**Publisher's note:** Springer Nature remains neutral with regard to jurisdictional claims in published maps and institutional affiliations.



**Open Access** This article is licensed under a Creative Commons Attribution 4.0 International License, which permits use, sharing, adaptation, distribution and reproduction in any medium or format, as long as you give appropriate credit to the original author(s) and the source, provide a link to the Creative Commons license, and indicate if changes were made. The images or other third party material in this article are included in the article's Creative Commons license, unless indicated otherwise in a credit line to the material. If material is not included in the article's Creative Commons license and your intended use is not permitted by statutory regulation or exceeds the permitted use, you will need to obtain permission directly from the copyright holder. To view a copy of this license, visit <http://creativecommons.org/licenses/by/4.0/>.

© The Author(s) 2017